Electron current extraction from radio frequency excited micro-dielectric barrier discharges

Jun-Chieh Wang,[1] Napoleon Leoni,[2] Henryk Birecki,[2] Omer Gila,[2] and Mark J. Kushner[1,a)]
[1]*Electrical Engineering and Computer Science Department, University of Michigan, 1301 Beal Ave., Ann Arbor, Michigan 48109, USA*
[2]*Hewlett Packard Research Labs, Palo Alto, California 94304, USA*

(Received 16 August 2012; accepted 20 December 2012; published online 16 January 2013)

Micro dielectric barrier discharges (mDBDs) consist of micro-plasma devices (10–100 μm diameter) in which the electrodes are fully or partially covered by dielectrics, and often operate at atmospheric pressure driven with radio frequency (rf) waveforms. In certain applications, it may be desirable to extract electron current out of the mDBD plasma, which necessitates a third electrode. As a result, the physical structure of the m-DBD and the electron emitting properties of its materials are important to its operation. In this paper, results from a two-dimensional computer simulation of current extraction from mDBDs sustained in atmospheric pressure N_2 will be discussed. The mDBDs are sandwich structures with an opening of tens-of-microns excited with rf voltage waveforms of up to 25 MHz. Following avalanche by electron impact ionization in the mDBD cavity, the plasma can be expelled from the cavity towards the extraction electrode during the part of the rf cycle when the extraction electrode appears anodic. The electron current extraction can be enhanced by biasing this electrode. The charge collection can be controlled by choice of rf frequency, rf driving voltage, and permittivity of the dielectric barrier. © *2013 American Institute of Physics*. [http://dx.doi.org/10.1063/1.4775723]

I. INTRODUCTION

Extraction of electron current from arrays of micro-plasma devices is attractive due to its potential application for surface treatment of large areas with high spatial resolution.[1,2] A number of microplasma configurations have been investigated, including the cathode boundary layer (CBL) discharge,[3] the capillary plasma electrode (CPE) configuration,[4–6] microhollow cathode discharges (MHCD),[7,8] and dielectric barrier discharges (DBDs).[9–12] DBDs are becoming a common microplasma device, particularly when operating at higher pressures (hundreds of Torr and above) due to their intrinsic stability against arcing. In fact, commercial plasma display panels use a DBD configuration, albeit on scales of hundreds of microns.[13]

DBDs have been developed as stable, high-pressure, and non-thermal plasma sources.[14] The plasma in DBDs is sustained between electrodes of which one is (or both are) covered by a dielectric. The electrodes are driven with alternating voltages of tens of Hz to as high as radio frequency (rf), MHz. Conventional DBDs with large area electrodes sustained at atmospheric pressure typically have gap spacings of a few mm. At low frequencies, the plasma in these devices operates in a filamentary mode with each individual filament having a diameter of tens to hundreds of μm. When operating at a high frequency (tens of kHz or above) or with rapidly rising voltage pulses in mildly attaching gas mixtures, DBDs often visually appear to be a uniform plasma since the rapid onset of voltage and preionization from the prior pulse tend to work against the formation of large filaments.[15,16]

When a DBD operates in a filamentary mode, upon initiation the filament propagates across the gap as a streamer. When the streamer strikes the opposite surface, it electrically charges the dielectric surface and so removes the local potential drop across the gap. As the gap voltage falls below its self-sustaining value, the plasma is quenched, thereby preventing the formation of an arc. The surface charges on the dielectrics, excited states, and ions left in the plasma channel are often referred to as microdischarge remnants.[17] When the polarity changes on the following half ac cycle, a more intense electron avalanche may occur at the same location due to the higher voltage across the gap from the previously charged dielectrics. At atmospheric pressure, particularly in attaching gases, the plasma formation and decay times can be as short as a few to tens of ns, whereas the ac period, even at rf frequencies, may be tens to hundreds of ns. As a result, the plasma may need to be re-ignited with each rf cycle.

Due to the unique features of being non-equilibrium and the ability to operate stably at atmospheric pressure and high power deposition, DBDs form the basis of a wide range of applications.[14,18] For example, ozone generation and remediation of toxic gases,[19,20] UV/VUV photon sources and polymer functionalization,[21–23] and plasma display panels[13,24] are typical DBD applications. Recently, DBDs are also being implemented as plasma sources in biomedical medical applications,[25,26] area-selective surface modification,[1,2,27] investigations of nonlinear behavior,[28] self-organized pattern formation,[29,30] and large arrays of DBDs having apertures of tens of microns as lighting sources.[9,11,12]

Our interest is in arrays of DBDs operated at atmospheric pressure which can be used as sources of electron current for patterning dielectric surfaces. In this application, charge is extracted out of a micro-DBD (or mDBD) having an electrode structure of tens of microns in size using an auxiliary

a)Author to whom correspondence should be addressed. Electronic mail: mjkush@umich.edu.

electrode separated by hundreds of microns.[31] These devices are capable of delivering narrow beams of extracted electron current tens of microns in diameter. Arrays of these mDBD devices can be used to form latent electrostatic images in the context of ion deposition printing, charge deposition printing, ionography, electron beam imaging, and digital lithography. This image transfer device may include, for example, laser printers, copiers, or facsimiles.[31–33]

On larger spatial scales, these 3-electrode configurations for microplasmas have been used at low pressure to extract charges or create plumes of excited states. For example, Pitchford *et al.*[34,35] demonstrated efficient production of $O_2(^1\Delta)$ in a three-electrode micro-cathode sustained discharge. This configuration consisted of a MHCD acting as a plasma cathode to maintain a stable glow discharge between the MHCD and a third, positively DC biased planar electrode a few mm away.[7] Müller *et al.*[36] demonstrated that one can use a large area plasma source on the basis of a surface discharge DBD system for the production and extraction of ions. A biased woven electrode is positioned on top of a flat disk of dielectric while the second grounded electrode is on its reverse side. A biased electrode in front of the DBD is used for extraction of ion current. Recently, a micro-plasma stamp[27] was developed based on the principle of mDBDs by Lucas *et al*. The plasma occurs in cylindrical cavities having dimensions as small as a few microns covered by the substrate to be patterned by the microplasma stamp. The substrate acts as an extraction cathode.

Despite the fact that the plasmas sustained in mDBDs are relatively straight forward to generate, maintaining the system in a stable region and obtaining accurate measurements of plasma parameters is complicated and challenging due to their small spatial and temporal scales. In order to provide insights to the nonlinear plasma kinetics under such conditions, numerical simulation models have been developed to investigate plasma dynamics and their scaling.[24,28,37–40]

In this paper, we present results of a numerical investigation of electron current extraction from a rf excited mDBD having an auxiliary electrode sustained in atmospheric pressure N_2. The mDBD device, shown in Fig. 1, consists of a cylindrical micro-cavity 65 μm in diameter in a grounded electrode, separated from a rf powered electrode by a dielectric sheet. The positively biased current extraction electrode is separated from the mDBD cavity by 400–500 μm. In this study, we parameterized the rf driving voltage, frequency, and dielectric constant of the insulator. We found that in properly designed devices, the vast majority of extracted current is produced in the mDBD cavity rather than in the gap between grounded electrode and top extraction electrode. Over the range of driving frequencies investigated (2.5 to 25 MHz), a pre-pulse and a single current pulse are produced at high frequency (10–25 MHz) which break into multiple current pulses at lower frequencies (2.5–5 MHz). Charge collection by the top biased electrode increases with increasing rf frequency, driving voltage, and dielectric constant of the insulator.

The model used in this investigation is described in Sec. II, followed by a discussion of the plasma dynamics and current extraction from mDBDs in Sec. III. In Sec. IV, the dielectric charging characteristics and ionization processes

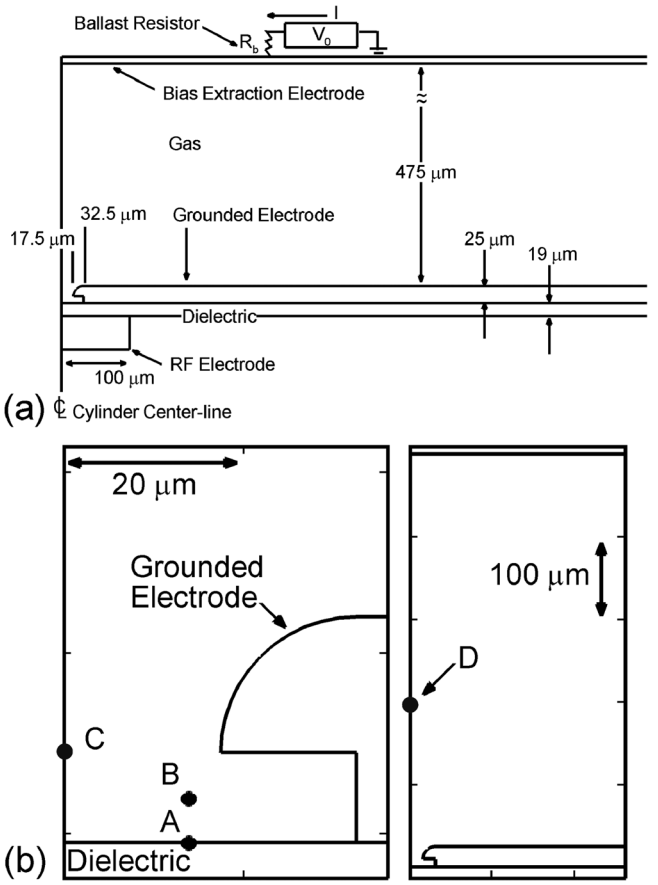

FIG. 1. Schematic of the cylindrical symmetric mDBD device. (a) Entire device and full computational domain. (b) Enlargement of mDBD cavity and location of sites A, B, C, and D that are used to provide surface properties and ionization characteristics.

in the mDBD cavity and gap are discussed. Charge collection by varying rf frequency, driving voltage, and dielectric constant is discussed in Sec. V. Sec. VI contains our concluding remarks.

II. DESCRIPTION OF THE MODEL

The model used in this investigation, *nonPDPSIM*, is described in detail elsewhere.[41,42] Briefly, *nonPDPSIM* is a two-dimensional, multi-fluid hydrodynamic simulation in which continuity equations and Poisson's equation are simultaneously solved for densities of all charged species (electrons and ions), the charge density (in and on materials), and electric potential. The time evolution of the charged species densities and surface charges are simultaneously integrated with Poisson's equation using a fully implicit Newton-Raphson iterative method. The electron energy equation for the bulk electron temperature and neutral continuity equations are then also implicitly solved. Rate coefficients and transport coefficients for bulk electrons are obtained from local solutions of Boltzmann's equation for the electron energy distribution (EED). Once the electric potential, charge density, and electron temperature have been updated, radiation transport is addressed by using Greens function propagator. The radiation is produced by relaxation of high-lying excited states of N_2. An electron Monte Carlo

simulation is applied to track the ionization sources produced by sheath-accelerated secondary electrons. Sources of secondary electrons include ion and photon fluxes onto surfaces. The differential equations are discretized using finite volume techniques, and the numerical grid uses a boundary fitting unstructured mesh with triangle elements with multiple refinement zones.

The fundamental equations we solved simultaneously for charged species are

$$-\nabla \cdot (\varepsilon \nabla \Phi) = \sum_j N_j q_j + \rho_s, \tag{1}$$

$$\frac{\partial N_i}{\partial t} = -\nabla \cdot \vec{\phi}_i + S_i, \tag{2}$$

$$\frac{\partial \rho_s}{\partial t} = \left[\sum_i q_i(-\nabla \cdot \vec{\phi}_i + \mathrm{S_i}) - \nabla \cdot (\sigma(-\nabla \Phi)) \right]_{material}, \tag{3}$$

where ε, Φ, ρ_s, N, ϕ, σ, S, and q refer to permittivity, electric potential, surface charge density, charged species number density, species flux, material conductivity, source terms, and elementary charge, respectively. The source term S_i includes the production and loss of species i due to electron impact excitation and ionization, heavy particle reactions, photo-ionization, secondary electron emission, field emission, and surface reactions. The charged species flux ϕ_i is discretized using the Scharfeter-Gummel scheme[43] providing an optimized approximation of drift-diffusion equation for charged particle transport—the flux has the properties of being upwind or downwind according to the direction and the magnitude of the drift flux compared to the diffusion flux. Once the charged particle density and electric potential are updated, the electron energy equation is solved for average energy ε

$$\frac{\partial (n_e \varepsilon)}{\partial t} = \vec{j} \cdot \vec{E} - \nabla \cdot \left(\frac{5}{2} \vec{\phi}_e \varepsilon - \lambda \nabla T_e \right) - n_e \sum_i \Delta \varepsilon_i k_i N_i,$$
$$\vec{j} = q_e \vec{\phi}_e, \tag{4}$$

where n_e is electron density, k_i is the rate coefficient for power loss for collision of electrons with species i having density N_i and electron energy loss $\Delta\varepsilon_i$, $\vec{\phi}_e$ is the electron flux, λ is electron thermal conductivity, and T_e is the electron temperature defined by $\varepsilon = 3T_e/2$. The electron transport coefficients and rate coefficients for use in solving Eq. (4) are obtained by solving Boltzmann's equation for the EED using a two-term spherical harmonic expansion for a wide range of values for E/N. A table of transport coefficients as a function of the resulting electron temperature T_e is then constructed, and is interpolated during execution of the code. This table is periodically updated as the composition of the electron collision partners varies.

We include electric field emission from metal surfaces in the model using the Richardson-Dushman equation to provide the locally emitted electron current density as function of the work function of the metal and the electric field at the surface of the metal. We found, however, that the electric fields produced during typical operation of the mDBD are insufficient to produce significant electric field emission and so electric field emission does not affect device performance.

Radiation transport is addressed by using a Greens function approach, the end product of which is photoionization in the gas phase and photoelectron emission from surfaces. In our model, the photo-ionization source ($\mathrm{cm^{-3}\ s^{-1}}$) for species i at location $\vec{r}_l$ resulting from photon emission by species j at location $\vec{r}'_m$ is

$$S_i(\vec{r}_l) = N_i(\vec{r}_l) \sum_j A_j \int \sigma_{ji} N_j(\vec{r}'_m) G_j(\vec{r}'_m, \vec{r}_l) d^3 \vec{r}'_m, \tag{5}$$

$$G_j(\vec{r}'_m, \vec{r}_l) = \frac{\exp\left(-\sum_k \int_{\vec{r}'_m}^{\vec{r}''_n} \sigma_{jk} N_k(\vec{r}''_n) d\vec{r}''_n \right)}{4\pi |\vec{r}'_m - \vec{r}_l|^2}, \tag{6}$$

where N_j is the radiating species density with Einstein coefficient A_j, and σ_{ji} is the photo-ionization cross section for species i by photons emitted from species j. In traversing the plasma, the photons are absorbed by species k with cross section σ_{jk}. This is addressed by the Green function propagator $G_j(\vec{r}'_m, \vec{r}_l)$ which accounts for the probability of survival of the photons emitted at $\vec{r}'_m$ to reach location $\vec{r}_l$ with absorption length λ_j. $G_j(\vec{r}'_m, \vec{r}_l)$ also accounts for physical obstructions and view angles which might block the radiation. In practice $G_j(\vec{r}'_m, \vec{r}_l)$ is computed only for a specified volume around $\vec{r}'_m$ which has a radius of 250 μm in this investigation. The same algorithm is used to generate secondary electrons by photoemission from surfaces. The flux of secondary electrons ($\mathrm{cm^{-2}\ s^{-1}}$) from surface location $\vec{r}_l$ is

$$\phi_S(\vec{r}_l) = \sum_j A_j \int \gamma_j(\vec{r}_l) N_j(\vec{r}'_m) G_j(\vec{r}'_m, \vec{r}_l) d^3 \vec{r}'_m, \tag{7}$$

where $\gamma_j(\vec{r}_l)$ is the photoemission probability for photon j.

An electron Monte Carlo simulation (EMCS)[44] is used to track the trajectories of secondary electrons emitted from surfaces. Based on local ion and UV photon fluxes and their secondary electron emission coefficients, electron pseudoparticles are released from numerical mesh nodes on surfaces. The trajectories of the sheath accelerated secondary electrons and their ionization progeny are tracked until they hit boundaries, move out of the region allocated for the EMCS region or fall below a specified energy, thereby being removed from EMCS, and join the bulk electron distribution. The pseudoparticle energies are recorded during their trajectories to compute EEDs for the secondary electrons as a function of position, and from the EEDs, electron impact source functions are computed. Electrons which are emitted from surfaces, called primary electrons and which represent injected current, which join the bulk electrons are recorded as sources of current and are included in the continuity equations for the bulk electron distribution. Primary electrons which strike surfaces are summed into sources for surface charging or, if the surface is an electrode, as a source of current. Secondary electron emission coefficients of 0.15 and 0.1 were used for all positive ions and photons, respectively, in this investigation.

The underlying computational mesh used in *nonPDPSIM* is unstructured, which makes integrating the trajectories of pseudo-particles in the EMCS difficult. To facilitate these integrations, a spatially fine Cartesian mesh is overlaid onto the unstructured mesh. Electric field quantities are interpolated onto the structured mesh for use in advancing the trajectories of the pseudo-particles. The EEDs and electron impact source functions are computed on the structured mesh. These results are interpolated back onto the unstructured mesh. The EMCS is called periodically during the simulation and the electric fields are held constant during that call to the EMCS. The source functions produced by the EMCS are then held constant in the remainder of the model until the EMCS is called again.

The mDBD geometry is shown in Fig. 1. A rf electrode with applied voltage from 1.4 to 5.6 kV and frequencies of 2.5 to 25 MHz is buried in a printed-circuit-board having relative permittivity $\varepsilon_r = \varepsilon/\varepsilon_0 = 4.3$. A grounded electrode 25 μm thick is separated from the rf electrode by a 19 μm thick dielectric sheet having ε_r up to 20. This dielectric layer is, in the model, a perfect insulator—the conductivity is zero so that the surface charges are laterally immobile on the dielectric sheet. In reality, we expect that there will be some photon generated conductivity. The cylindrically symmetric mDBD cavity is 65 μm in diameter with a 35 μm diameter opening. The top extraction electrode is biased with up to 2 kV and is separated from the grounded electrode by a 475 μm gap. A 100 kΩ ballast resistor is connected to the extraction electrode to limit the current and so prevent arcing. There are 5700 computational nodes in the mesh of which 2800 are in the plasma zone. The typical mesh spacing is 2 μm in the microdischarge cavity and 12 μm in the gap. Although the mDBDs are typically used in arrays, we report on here on the scaling of a single cylindrically symmetric device. Our investigation of small arrays of devices will be reported elsewhere.

The gas fill is 1 atm of N_2 with a small amount of O_2 as an impurity—$N_2/O_2 = 99.99/0.01$ at 300 K. This impurity reflects the estimated purity of the gas used in experiments. Including a small amount of O_2 impurity also provides an unambiguous species which can be photoionized. Due to the magnitude of the calculation, we used a reduced reaction mechanism containing a subset of the reactions described in Refs. 45 and 46 to minimize the computation time while capturing the dominant plasma hydrodynamics and chemistry. The reduced reaction mechanism includes N_2, $N_2(v)$, N_2^*, N_2^{**}, N_2^{***}, N_2^+, N_4^+, N, N^*, N^+, O_2, $O_2(^1\Delta)$, O_2^+, O_2^-, O_3, O^-, O, $O(^1D)$, O^+, and electrons. The states N_2^* and N_2^{**} are nominally N_2(A,B) and N_2(C) though the latter is treated as a lumped state including transitions higher than N_2(C), and N_2^{***} is nominally $N_2(a')$ and higher states.

The discharge is initiated by placing an electrically neutral electron-ion cloud centered in the mDBD cavity with peak density 10^{12} cm^{-3} and 100 μm in radius. The precise density and radius of the initiating cloud does not affect the predicted operation of the device except during the first half cycle. A succession of rf cycles (referred to as pulses) are then computed. The time step is chosen dynamically and is typically 6×10^{-12} s during the high voltage portion of the cycle and 10^{-11} s during the low voltage portion of the cycle. Many rf cycles are computed until either quasi-steady state conditions are achieved or long term trends are discernable.

Although the gas temperature is held constant during the simulation, it is true that local gas heating can produce temperature excursions in pulsed microplasma devices. The dominant heating mechanisms are ion acceleration followed by charge exchange reactions and Franck-Condon heating following dissociative excitation during the current pulse. V-T relaxation of vibrationally excited states also contributes to gas heating after the current pulse. Since the current pulse is short compared to the entire pulse period, the large surface-to-volume ratio of these devices enables rapid heat transfer to the walls. This is facilitated by the majority of the heating occurring close to boundaries. As such, we do not expect large temperature excursions.

III. PLASMA DYNAMICS AND CURRENT EXTRACTION FROM THE mDBD

The characteristic of mDBD current extraction for a frequency of 25 MHz (pulse period of 40 ns) will first be discussed. The sinusoidal rf voltage amplitude is 1.4 kV and the top extraction voltage is 2 kV. The dielectric constant for the insulating sheet is $\varepsilon_r = 20$. The time evolution of E/N (electric field/gas number density) and electron density in the mDBD cavity are shown in Fig. 2 over a single cycle during the pulse periodic steady state. The electron density in the plume of extracted current is shown in Fig. 3. The electron temperature T_e, and electron impact ionization sources by bulk electrons, S_e and secondary electrons S_{sec}, are shown in Fig. 4.

The peak electron density, n_e, within the mDBD cavity is approximately 3.2×10^{15} cm^{-3}, a value that is maximum when the potential on the rf electrode crosses zero toward negative values. The change of n_e in the mDBD cavity during the cycle is over a factor of 100. n_e in the electron plume has a maximum value of 2.5×10^{12} cm^{-3} 220 μm above the mDBD cavity to 10^{12} cm^{-3} 28 μm below the collection electrode, corresponding to that time when the rf voltage crosses zero towards negative values. The electron density decays to negligible values within 15 ns of the peak as electrons are swept out of the gap into the collection electrode.

During the negative portion of the rf cycle, the positive ions in the mDBD cavity drift towards the dielectric and positively charge it. When the rf potential (V_{rf}) crosses from negative to positive at the beginning of the cycle (t = 0 ns in the figures), the net voltage between the top extraction electrode and the now positive dielectric is small due to the previous positive charging of the dielectric. The electrons in the mDBD drift towards the dielectric and begin to neutralize the positively charged dielectric. Before the positive peak of V_{rf} at t = 10 ns, the negative charge collected on the dielectric has neutralized a sufficient amount of the positive charge that there is a net extracting field that accelerates electrons out of the mDBD cavity. A small flux of electrons, the pre-pulse, escapes from the cavity, and is accelerated across the gap by the extraction electrode. This pre-pulse is magnified with large values of dV/dt hence is more prominent at higher rf frequencies.

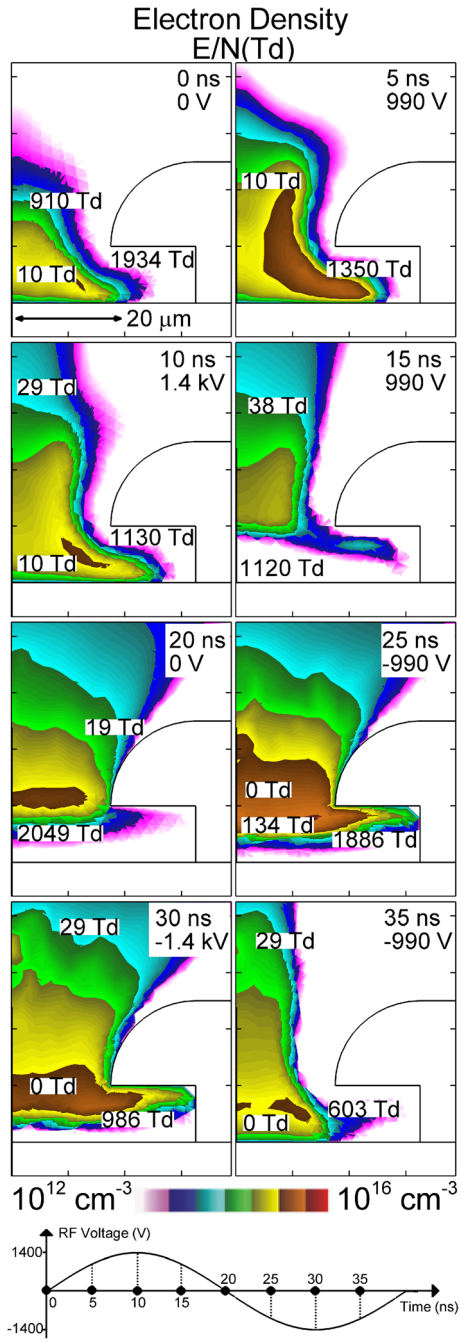

FIG. 2. Time evolution of electron density (log scale, cm^{-3}) and E/N (at the center of contour labels, Td) in the mDBD cavity at different phases of the rf driving voltage of 1.4 kV during a 40 ns (25 MHz) cycle. The cycle begins with 0 V on the buried rf electrode. The top electrode is biased with +2 kV. At high electron density, the electric field is shielded and E/N is reduced.

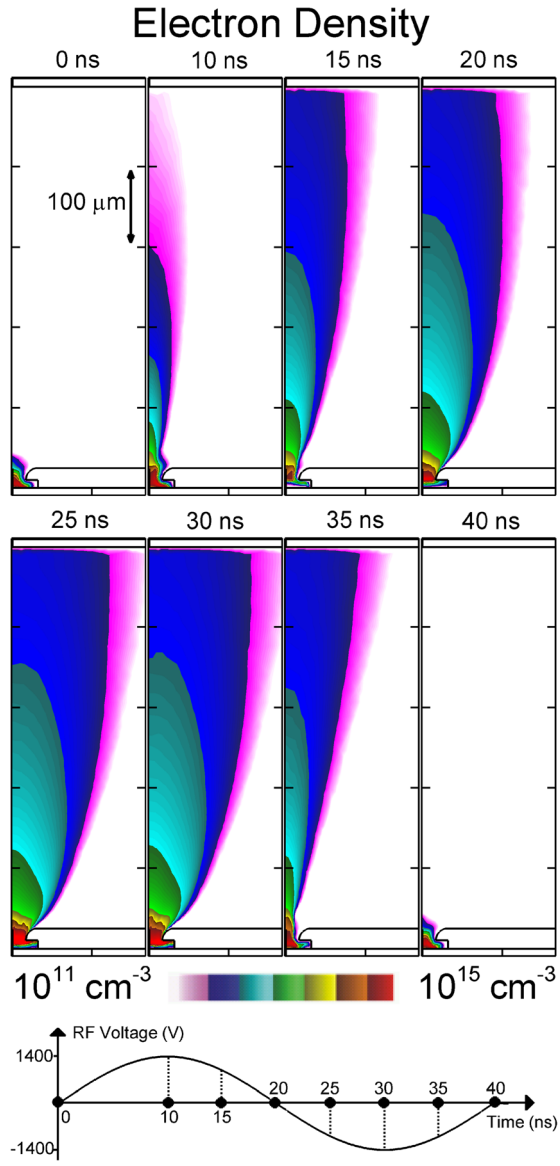

FIG. 3. Electron density in the plume (log scale, cm^{-3}) in the gap at different phases of the rf driving voltage of 1.4 kV during a 40 ns (25 MHz) cycle.

When V_{rf} decreases to zero at t = 20 ns, a negative potential still exists on the dielectric due to the previous collection of electrons. At this point, the extraction field is at maximum and an electron plume is then extracted from the cavity, which reduces the electron density in the mDBD cavity. At the same time, S_e and S_{sec} reach their maximum values ($10^{25}\,cm^{-3}\ s^{-1}$), a consequence of an avalanche of remaining residual electrons in the mDBD cavity and by secondary electrons emitted from surfaces in the cavity. This in-cavity avalanche then enhances the current extraction to the top biased electrode. The electron plume reaches its greatest extent at 30 ns at the negative peak of V_{rf}. As this proceeds, positive ions are being collected on the dielectric, which reduces the voltage drop across the gap. The electron plume then begins to diminish and nearly extinguishes. The cycle then restarts.

The electron plume is essentially extinguished every rf cycle and so requires re-ignition each cycle. This re-ignition process is facilitated by the dynamics of E/N in the cavity. At the zero-crossing of V_{rf} at t = 0 ns, electrons are attracted to the center of the dielectric. This conductive plasma then shields out and reduces the electric field, which in turn reduces the electron temperature T_e and S_e—they are only significant in the vicinity of the vertex of the grounded electrode where S_e up to $2.5 \times 10^{24}\,cm^{-3}\ s^{-1}$ is produced. After the electron plume is extracted out of the cavity at t = 20 ns, the electron density is reduced which enables the voltage that was previously confined to the sheath to be dropped across the mDBD cavity. This enables a high T_e which avalanches the small remaining electron density,

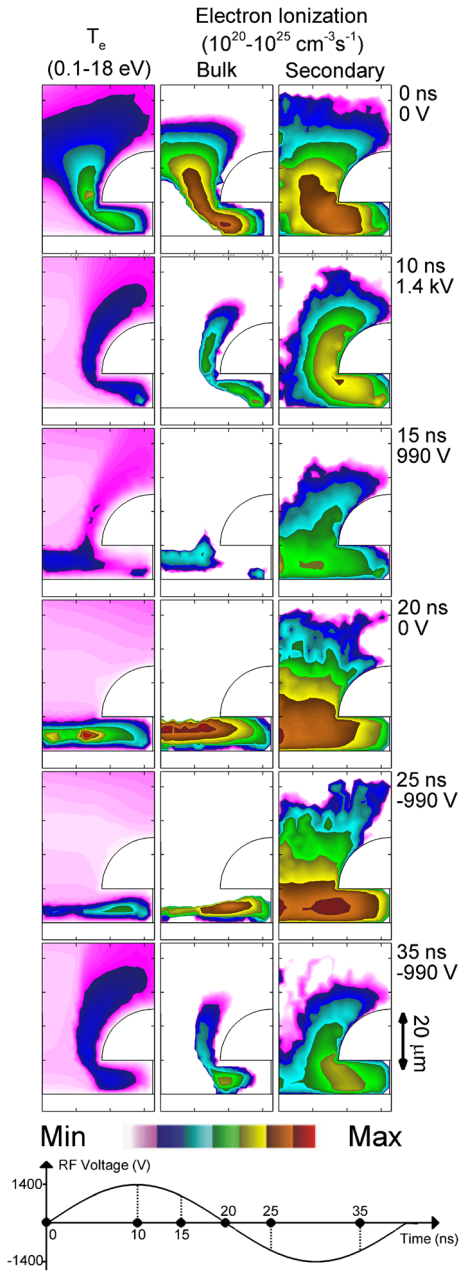

FIG. 4. Electron temperature (eV), electron impact ionization sources from bulk electrons (S_e), and ionization source by sheath accelerated secondary electrons (S_{sec}) in the mDBD cavity during a 40 ns (25 MHz) cycle for $V_{rf} = 1.4$ kV and extraction voltage of 2 kV. The ionization sources are plotted on a log scale.

proving a source as high as $3.8 \times 10^{24}\,\mathrm{cm}^{-3}\,\mathrm{s}^{-1}$. This avalanche enhances the electron plume and current extraction to the top biased electrode until the negative peak of V_{rf} is reached. Shortly after the negative peak in V_{rf} at t = 35 ns, the electron flux is attracted to the center of dielectric, and the conductive plasma shields the electric field, which reduces the ionization source. At this point, the ignition phase re-starts.

During the rf cycle, S_e and S_{sec} are synchronized with the dynamics of T_e. The secondary electron ionization source S_{sec} extends over a larger volume than S_e due to the longer mean free paths for the high energy electrons produced in the sheath compared to the bulk electrons accelerated in the volume. S_{sec} is also enhanced by a nearly continuous flux of UV photons incident onto all surfaces inside the mDBD cavity, including the dielectric, as discussed below.

The total charge density (ρ), positive, and negative charges are shown in Fig. 5. Excited states $N_2(C)$ and $N_2(A,B)$ density are shown in Fig. 6. Before 10 ns, there is net positive charge on the dielectric and in the vicinity of the vertex of ground electrode. Secondary electrons released from the grounded electrode are due to positive ion bombardment and photons. The net positive charge on the dielectric transitions to negative charge within 10 ns. As the electrons are extracted from the cavity at t = 20 ns, positive ions strike the negatively charged dielectric, releasing secondary electrons. As a result, the secondary electron ionization source peaks near the discharge electrode and negatively charged dielectric when they behave cathodically. In addition to positive ions producing secondary electrons which, upon sheath acceleration, produce ionization, UV photon emission from

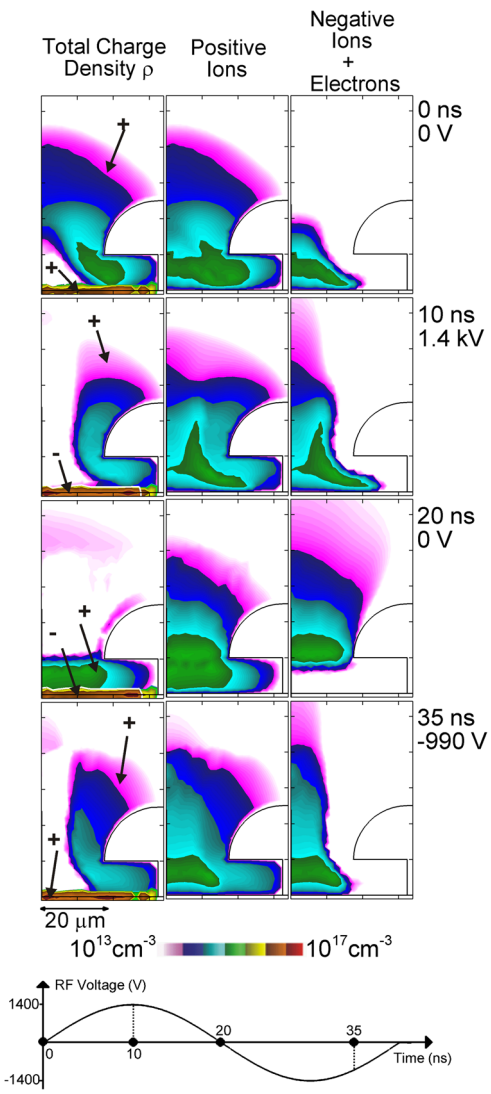

FIG. 5. The total charge density, charge density due to positive ions, and charge density due to electrons and negative ions (log scale cm^{-3}) in the mDBD cavity at different times during a 25 MHz cycle for $V_{rf} = 1.4$ kV and extraction voltage of 2 kV. Positive ions alternately strike the cathode-like negatively charged dielectric or discharge electrode and release secondary electrons for re-ignition.

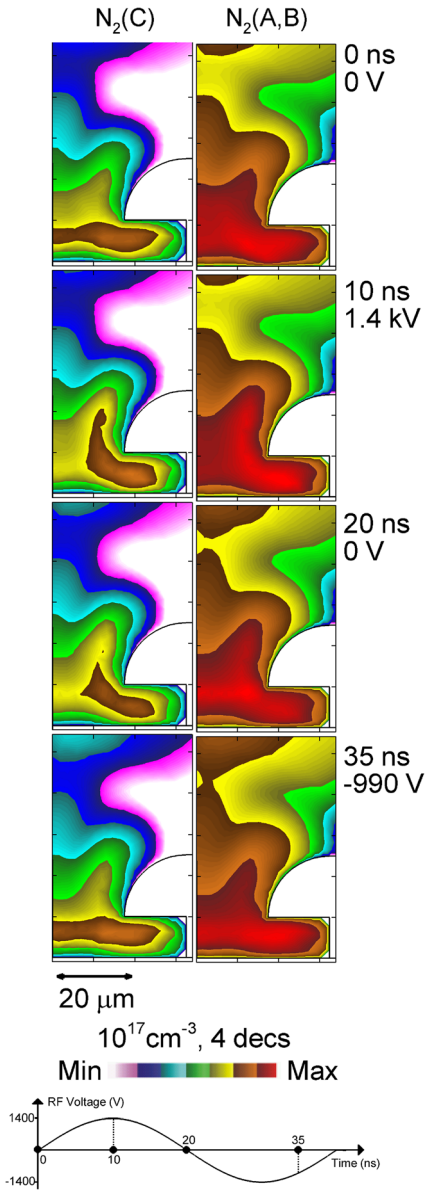

FIG. 6. Density of excited states $N_2(C)$ and $N_2(A,B)$ in the mDBD cavity (log scale, cm^{-3}) at different times during a 25 MHz cycle for $V_{rf} = 1.4$ kV and extraction voltage of 2 kV. UV photons emitted from excited states of nitrogen produce secondary electrons which aid in re-ignition of the plasma especially at low frequency.

excited states of nitrogen also helps seed the secondary electrons and re-ignite the avalanche. There can also be secondary emission from the flux of long lived excited states to these surfaces. Since the effective lifetimes of excited states are long compared to the intrapulse dynamics, at least for 25 MHz, there is a nearly continuous flux of UV photons which produce secondary electrons within the mDBD cavity. If produced during the anodic cycle (for that surface), these secondary electrons are accelerated back into the surface with little change in local plasma properties. If produced during the cathodic part of the cycle, the secondary electrons are accelerated by the sheath, and produce ionization throughout the volume of the mDBD cavity. Since S_{sec} is to some degree decoupled from the incident ion flux due to the availability of UV light, S_{sec} responds more quickly to changes in local electric field. These long lived neutral excited states become more important at lower frequencies for re-ignition when the mDBD cavity is more depleted of seed electrons.

IV. DIELECTRIC CHARGING CHARACTERISTICS AND IONIZATION PROCESSES

As points of reference, plasma properties will be discussed for the four sites (A, B, C, and D) placed on the surface of the dielectric, in the cavity and in the gap, as shown in Fig. 1(b). The surface charge density σ_S, and the electron density, ionization source, and E/N at sites A and B are shown in Figs. 7 and 8 for discharges in 1 atm of N_2 for frequencies ν_{rf} of 2.5 MHz to 25 MHz. For ν_{rf} up to 25 MHz, σ_S on the dielectric is nearly 180° out of phase with V_{rf}. This is largely expected as the dielectric sheet behaves as a capacitor and the frequency is high, which maximizes the displacement current. However, due to the power dissipation in the device, this is not a purely capacitive system, and so there is a phase delay between V_{rf}, dielectric charging and surface potential. At 25 MHz, when V_{rf} increases to its positive peak at $t = 10$ ns, the negative charge density on the dielectric also reaches its peak value. However, the surface potential on the dielectric is still positive. Then σ_S slowly decreases (becomes less negative) with decreasing rf voltage. During this time, the positive potential on the dielectric decreases towards zero and then changes its polarity to negative. As the rf voltage reduces to nearly zero at $t = 20$ ns, a negative potential up to -500 V is produced due to the previously collected negative surface charges. In comparison, the discharge electrode behaves anodically to enable an electron avalanche and a large electron plume is expelled from the microdischarge cavity. When V_{rf} changes its polarity to negative, positive ions are drawn into the dielectric which charges it positively. The negative potential on the dielectric is increased (become less negative) and then transitions to positive values.

Over the range of frequencies investigated, this charging cycle does not dramatically change. However, as the frequency decreases, structure is produced in the local dielectric potential and σ_S. This oscillating structure can be attributed to *overshoot*. Since the capacitance of the dielectric is fixed, there is a finite amount of charged particle fluence (either negative or positive) required to change the potential on the dielectric by a given amount. (Fluence, cm^{-2}, is flux integrated over time.) When this critical fluence is collected, the local potential of the dielectric builds to a sufficiently large value that it begins to retard the flux. At high frequencies, these time scales correspond to the rf period, and so there is a smooth transition from positive to negative dielectric potential. At lower frequencies, however, these dielectric charging times are shorter than the rf period. So the retarding potential on the dielectric slows down the collection of negative (or positive) charges at a time that V_{rf} is still increasing (or decreasing). The still increasing (or decreasing) V_{rf} then restarts the charge collection which produces the local minimum in the surface potential.

In addition to *overshoot* in surface charging, periodic bursts of ionization can lead to multiple peaks in current extraction. V_{rf}, local potential, E/N, electron density, and ionization source at site B are shown in Fig. 8 for ν_{rf} of

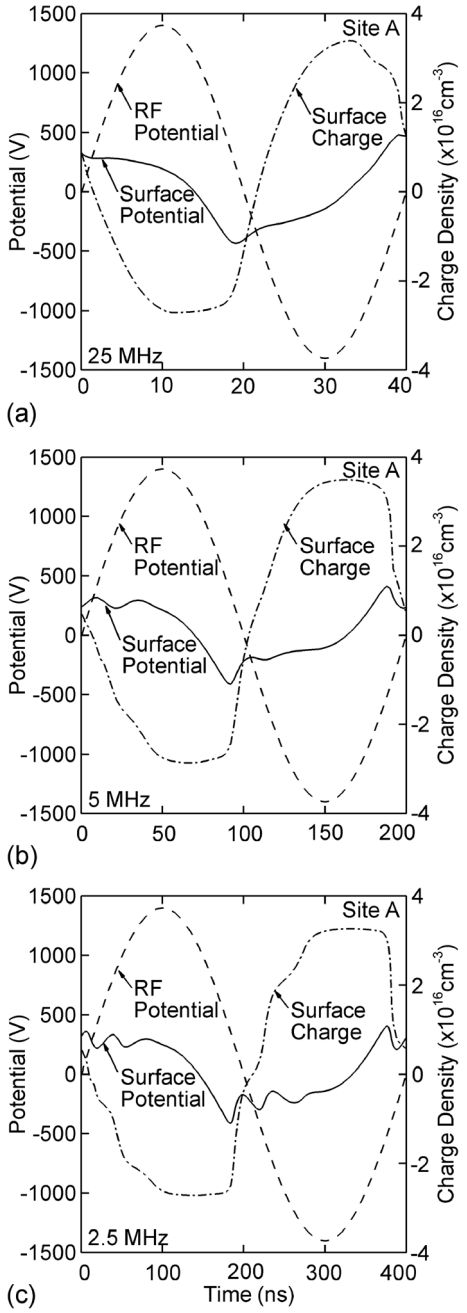

FIG. 7. The surface charge density σ_S (dashed-dotted, cm^{-3}), surface voltage on the dielectric (solid, V), and voltage on the buried rf electrodes (dashed, V) are shown for frequencies of (a) 25, (b) 5, and (c) 2.5 MHz at site A (see Fig. 1) for $V_{rf} = 1.4$ kV and extraction voltage of 2 kV. Oscillations in charging of the dielectric appear at low frequencies.

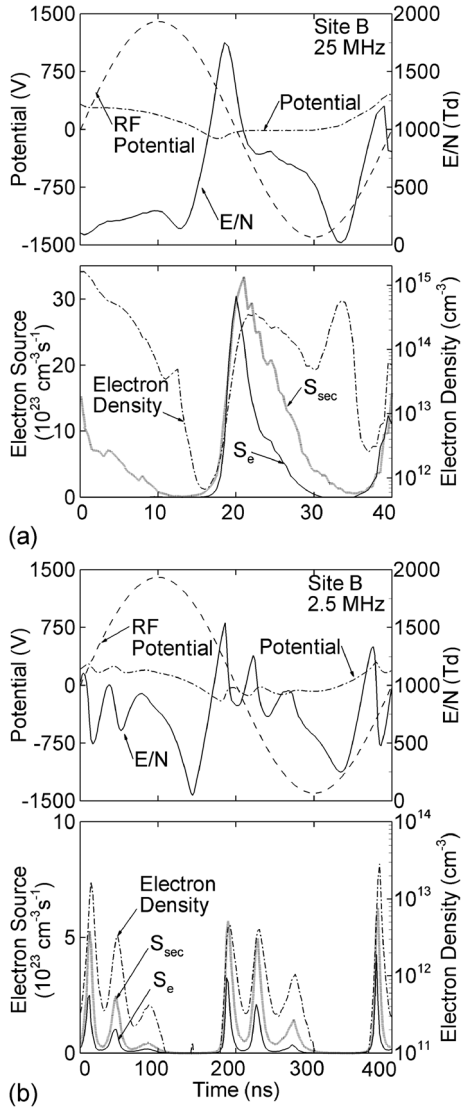

FIG. 8. mDBD characteristic are shown at site B as a function of time (see Fig. 1) for $V_{rf} = 1.4$ kV and extraction voltage of 2 kV for (a) 25 MHz and (b) 2.5 MHz: rf voltage (dashed, V), local potential (dashed-dotted, V), and *E/N* (solid, Td), electron density (dashed-dotted, cm^{-3}), and electron ionizations source S_e and S_{sec} (solid and dotted, $cm^{-3}\ s^{-1}$).

25 and 2.5 MHz. Corresponding extracted currents collected on the top electrode are shown in Fig. 9. At 25 MHz, a pre-pulse electron current of 0.3 mA is collected by the extraction electrode which is then followed by a larger main current pulse. This pre-pulse is correlated with large values of dV/dt and occurs before the zero-crossing of rf voltage at 20 ns. As the frequency decreases to 15 MHz, the pre-pulse is reduced to 0.1 mA and by 5 MHz, the pre-pulse is suppressed. Before the rf voltage changes its polarity to negative, the local potential in the cavity reaches its negative peak which increases *E/N* and the ionization sources (S_e and S_{sec}) in the mDBD cavity. This ionization provides the electron source for the main current pulse. At 25 MHz, for example, the local peak in *E/N* in the mDBD cavity reaches as high as 1700 Td (1 Td [Townsend] $= 10^{-17}$ V cm^2) slightly before V_{rf} zero-crossing at 20 ns, and the peak electron source exceeds $3 \times 10^{24}\ cm^{-3}\ s^{-1}$. The corresponding electron density then reaches $3.5 \times 10^{14}\ cm^{-3}$. The conductive, high electron density plasma in the cavity then shields out the electric field, *E/N* decreases which then decreases the electron sources. At all frequencies, the magnitudes of S_e and S_{sec} are commensurate with each other, with S_{sec} lasting somewhat longer due to the long lived excited states which, though photoelectron production, continue to seed secondary electrons at surfaces. For example, at 25 MHz the peak electron source from bulk plasma ionization (S_e) is essentially the same as that from secondary electron ionization (S_{sec}), on the order of $3 \times 10^{24}\ cm^{-3}\ s^{-1}$.

Shortly after the negative peak in V_{rf} at 30 ns, the local potential at site B becomes more positive due to the positive

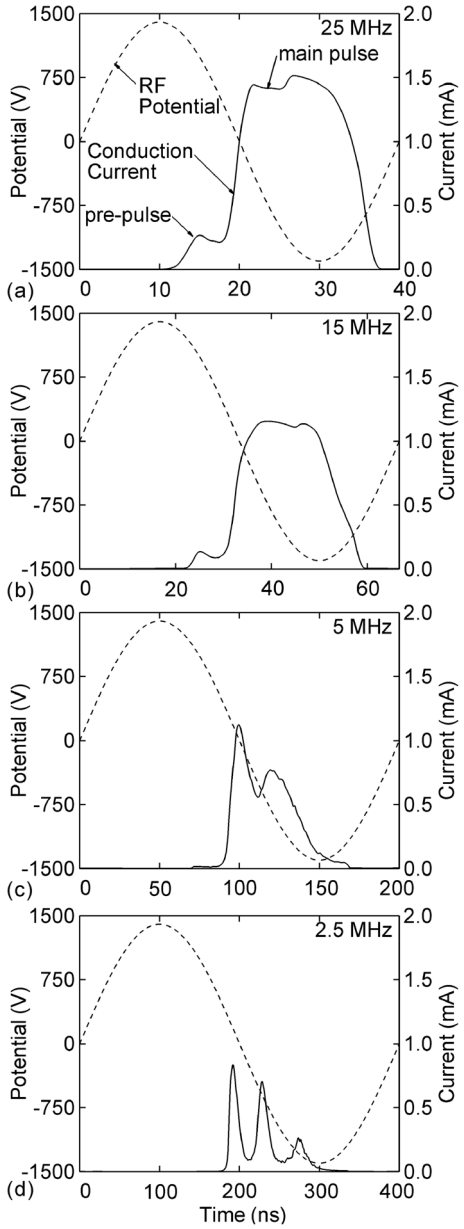

FIG. 9. rf potential (dashed, V) and collected current (solid, mA) for $V_{rf} = 1.4$ kV and extraction voltage of 2 kV. (a) 25 MHz, (b) 15 MHz, (c) 5 MHz, and (d) 2.5 MHz. The current transitions from a single pulse to multiple pulses as the frequency decreases.

surface charges, the electron plume begins to extinguish and electron flux is attracted to the dielectric. As the frequency decreases and the period becomes longer, there is sufficient electron current extracted to deplete the cavity. The local *E/N* then rebounds, which produces ionization sources, which in turn repopulate the electron density in the cavity which enables another burst of electron current to be collected. If V_{rf} has not yet changed sign, the process can repeat itself.

For example, at 2.5 MHz, the period of 400 ns is sufficient for multiple cycles of electron depletion and avalanche to occur. As shown in Fig. 8, depletion of electrons in the mDBD cavity as V_{rf} crosses zero towards negative values at 200 ns produces a peak in *E/N* of 1540 Td. This produces a burst of ionization which repopulates the mDBD cavity but also reduces *E/N* to about 850 Td These electrons are extracted producing the first current pulse (see Fig. 9) with the local electron density decreasing from 4×10^{12} cm^{-3} to 3×10^{11} cm^{-3}. The *E/N* then recovers to 1260 Td, the electron source follows *E/N*, and then a second local peak in electron density is formed for the second current pulse. The process repeats a third time before V_{rf} changes sign. The re-ignition of the plasma following each extraction is facilitated by a quasi-dc production of secondary electrons from the dielectric and grounded electrode by UV photons from long lived excited states. Note that the same process occurs on the anodic part of the rf cycle, producing peaks in the *E/N*, electron density, and ionization sources. These undulations are not reflected in the electron current collected at the top electrode since the net field is pointing in the opposite direction—the bursts of electron current are collected on the dielectric surface.

In general, S_e and S_{sec} follow *E/N* during a rf period for both 25 and 2.5 MHz, while S_{sec} is longer-lived in the cavity. However, for 25 MHz when V_{rf} cross zero at t = 0, S_{sec} is as large as 1.6×10^{24} cm^{-3} s^{-1} but S_e is negligible at site B, as shown in Fig. 8(a). At this time, electrons are attracted to the center dielectric due to the previous positive surface charging and the highly conductive plasma shields the local electric field, which results in the small bulk ionization source. At this time, however, a large amount of ionization by secondary electron ionization occurs near the vicinity of the tip of the discharge electrode, boosting S_{sec}, as the electrode behave cathodically.

Note that the peaks S_e and S_{sec} are on the order of 5×10^{23} cm^{-3} s^{-1} at 2.5 MHz which is 6 times smaller than the peak electron ionization sources at 25 MHz. The lower electron source at 2.5 MHz can be attributed to the lower residual electron density in the cavity surviving from the prior pulse. At 2.5 MHz, the period is long enough that the majority of electrons are extracted out of the cavity. Positive ion and UV fluxes from long lived excited states can facilitate re-ignition at 2.5 MHz by production of secondary electrons from surfaces. However, these secondary electron sources are too small to trigger as large an avalanche as that produced by the higher residual electron density at 25 MHz. As a result, the peak current collection tends to decrease with decreasing frequency.

The trends in extracted and collected current from 25 and to 2.5 MHz include the loss of the pre-pulse, due in large part to the decreasing dV/dt at low frequency, and the onset of modulation in the current at low frequency due to the cycle of extraction, depletion, and avalanche. Similar trends of oscillating currents (single current pulses at high frequency, multiple current pulses at low frequency) in DBDs were reported in the modeling results by Petrović *et al.*,[37] and in the experimental results by Radu *et al.*[47] and Shin and Raja.[38] These oscillations were reported for larger parallel plate devices and at lower frequencies (kHz). However, the basic sequence of events is similar—charging, depletion, ionization, extraction.

Multiple pulses of current at 2.5 MHz are also experimentally observed when using the same sandwich mDBD configuration of slightly different size and operated under similar conditions. In the experiment, the top extraction

electrode is grounded, a −1 kV DC voltage is applied to both rf and discharge electrodes, while rf electrode is also biased with a 1 kV ac voltage at 2.5 MHz. The experimental voltage drop between the rf and discharge electrode and current collection on the top electrode are shown in Fig. 10(a). From a biasing standpoint, this arrangement is equivalent to that used in the simulated results shown in Fig. 10(b). The results from the simulation are in basic agreement with the experiment data, although the current is smaller in the experiment which can be attributed to differences in geometry and operating conditions. The predicted triple pulses of current extracted at the zero crossing of the rf voltage are corroborated by the experiment. The transition from triple pulses to double pulses is observed both experimentally and computationally.

Recall that the top electrode is biased positively and there is a ground electrode at the top of the mDBD cavity. Although the current flowing from the buried rf electrode having a rf bias must be ac, there is no requirement that the current flowing to the top electrode is ac since there is a non-capacitive path to ground through the top electrode. If the potential drop between the top extraction electrode and ground electrode is large enough there could be a dc discharge, and an optimally designed device would either avoid this possibility with a lower extraction voltage, or limit the current with an appropriate ballast resistor. Even with a less than self-sustaining voltage on the extraction electrode, it is possible to have a quasi-dc current by virtue of the electrons injected into the gap from the mDBD cavity. The dc discharge between the grounded and top extraction electrode would then operate as an externally sustained discharge, in analogy to, for example, electron beam sustained discharges.[48]

To illustrate these scalings, the electron and positive ion density at site D (see Fig. 1(b)), and extracted electron current are shown in Fig. 11 as a function of extraction voltage on the top electrode for 25 MHz excitation on the rf electrode. With a 1 kV extraction voltage, the current on the top electrode consists of a series of pulses. The time averaged *E*/*N* (80 Td) across the gap is too small to self-sustain (or avalanche) a discharge, and so current is collected only when electrons are extracted from the mDBD cavity. The probability of recombination and attachment for this gas mixture during the transit time across the gap is small, and so the majority of the extracted current out of the mDBD cavity is swept to the top electrode. The *E*/*N* is small enough that there is only a small amount of ionization and positive charge generated in the gap.

For a 2 kV extraction voltage, the collected electron current begins as being purely pulsed, which reflects the periodic extraction of electrons from the mDBD cavity. With this time averaged *E*/*N* (170 Td), there is non-negligible ionization within the gap, which has two consequences. First, the pulsed current extracted from the mDBD cavity is amplified in crossing the gap, as shown by the pulses prior to 400 ns.

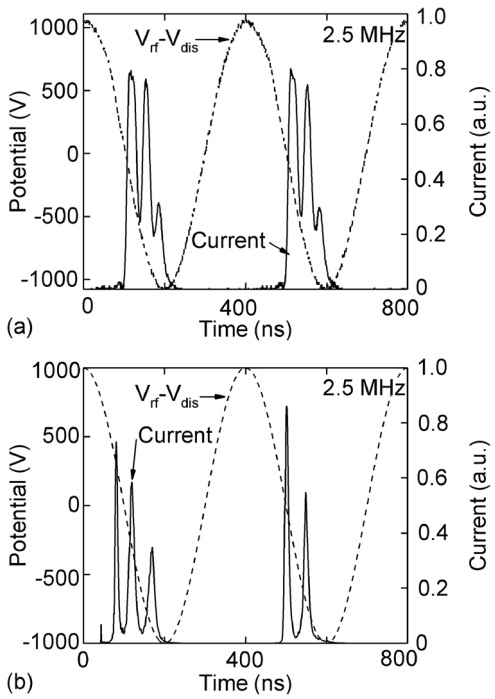

FIG. 10. Current collection on the top electrode. (a) Experimentally observed triple current pulsed obtained at 2.5 MHz and (b) simulation results in a similar sandwich mDBD device for equivalent biasing.

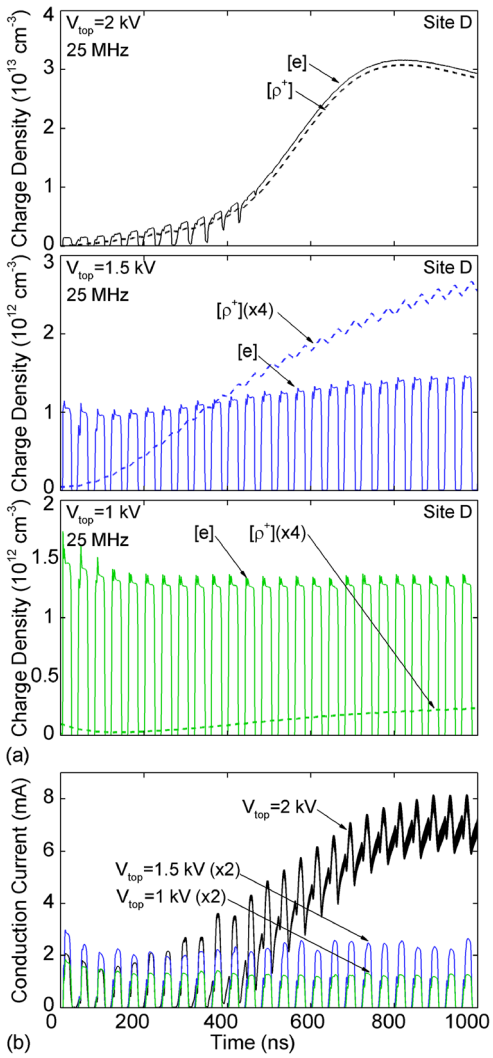

FIG. 11. Charge density at site D and current collection on the top electrode at 25 MHz. (a) Electron (solid, cm^{-3}) and positive ion density (dashed, cm^{-3}) at site D for top bias voltage V_{top} = 2, 1.5, and 1 kV. (b) Electron current collected by the top biased electrode for V_{top} = 2, 1.5, and 1 kV. A pulsed modulated dc current is collected at V_{top} = 2 kV.

Second, ionization and excitation in the gap increases the positive ion density, dominated by N_4^+ for these conditions, and excited state density. (The negative ion density due to the O_2 impurity is generally at least 2 orders of magnitude smaller.) The positive ions have a much lower drift velocity towards the grounded electrode and so are not highly modulated during the rf cycle. A transition occurs in the current collected by the top electrode to a pulsed modulated dc current. At this time, the gradually increasing positive ions perturb the local electric field, voltage, and charge collection until it reaches an oscillatory steady state. On a pulse-to-pulse basis, positive ions accumulate in the gap over time, as these heavier positive ions are not able to respond to the instantaneous electric field and create a local positive potential which enhances the extraction of charge from the gap. The accumulating excited states also increase the efficiency of ionization through multistep collisions. With a 2 kV extraction bias, the positive charge density ρ^+ at site D increases monotonically until reaching a steady state at 800 ns, which leads to a pulsed modulated dc current. This pulsed modulated dc current can be avoided by using a lower extraction voltage. For example, purely pulsed electron currents are collected by applying 1 and 1.5 kV top extraction voltages, as shown in Fig. 11(b).

V. TOTAL CHARGE COLLECTION

Total charge collected per pulse and time integrated charge collection on the top electrode as a function of time for rf frequencies of 2.5 to 25 MHz are shown in Fig. 12. The top extraction electrode is biased with +2 kV. For early pulses and lower frequencies, the charge per pulse collected is essentially the same, 3.5×10^{-11} C/pulse, and limited by the capacitance of the dielectric layer above the rf electrode. Although more peak current is collected at higher frequency, as shown in Fig. 9, more charge per pulse is collected by operating at lower frequency due to the longer charge extraction period and multiple current pulses per rf cycle. Integrated charge as a function of time at 25 MHz is higher due simply to the higher repetition rate. For frequencies greater than 10-15 MHz, charge collection per pulse is limited by the shorter rf period. The charge/pulse increases with number of the pulses until a quasi-dc condition is reached due to the accumulation of excited states and ions in the gap. At this point quasi-dc current is collected.

Integrated charge collection as a function of time for different rf voltages (1.4 to 5.6 kV) at 25 MHz is shown in Fig. 13. The corresponding dielectric properties (V_{rf}, surface charge and surface potential) at site A and ionization characteristics (E/N, electron density, and ionization sources) at site B are shown in Fig. 14. The magnitude of the charging of the dielectric scales nearly linearly with V_{rf}, as the discharge is dominantly capacitive—the charged particle flux to the intervening dielectric is that value that charges the dielectric to V_{rf}. The nearly linear increase of collected charge with voltage is less clearly correlated with this capacitive current. In general, electron density, E/N, and ionization sources at site B tend to increase with rf voltage. However, as the electron density increases, the local value of E/N decreases due to plasma shielding. In spite of this shielding, the electron impact sources by both bulk and sheath accelerated electrons increase with applied voltage due to non-local electron transport. The heating of electrons at the boundaries of the microcavity by the larger sheath electric fields (either by bulk Joule heating or secondary electron acceleration) convects into the center of the mDBD cavity to increase ionization rates.

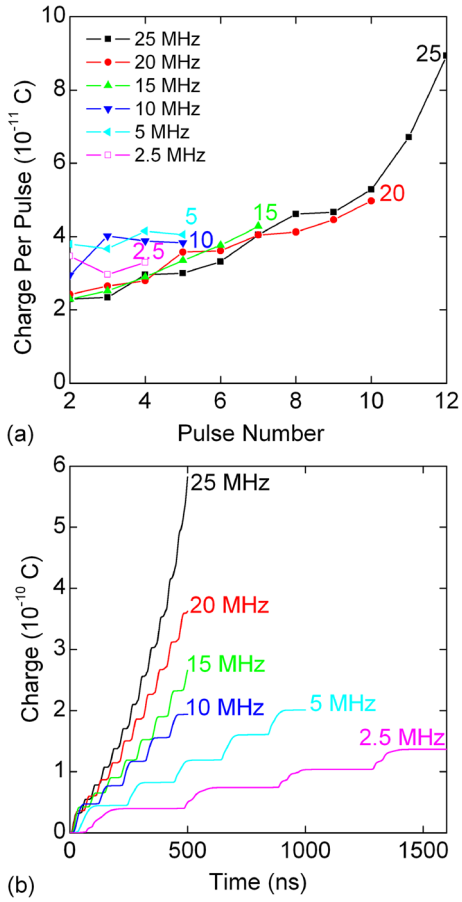

FIG. 12. Charge collection as a function of time for 25 MHz to 2.5 MHz (1.4 kV rf bias) and a 2 kV biased collection electrode. (a) Charge collected per pulse and (b) time integrated charge collection. Charge collection per pulse is relatively independent of frequency until positive charge builds up in the gap at the higher frequencies, which then transitions to a modulated dc discharge.

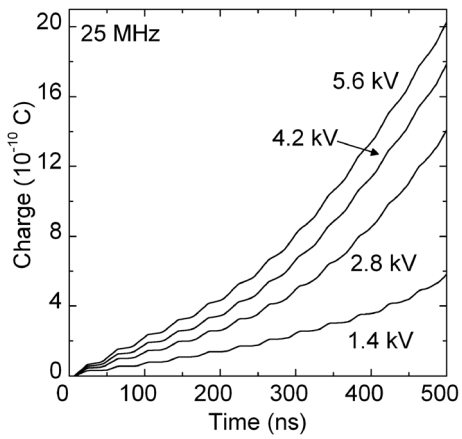

FIG. 13. Charge collection as a function of time for 25 MHz at $V_{rf} = 1.4$, 2.8, 4.2, and 5.6 kV and a 2 kV biased collection electrode.

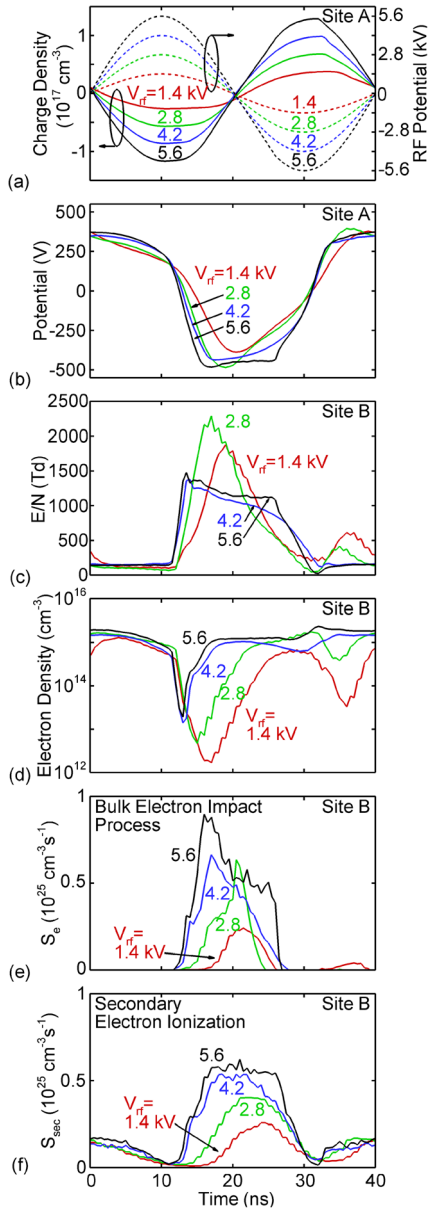

FIG. 14. Surface properties at site A and gas phase properties at site B as a function of time at 25 MHz for $V_{rf} = 1.4$, 2.8, 4.2, and 5.6 kV. The location is noted in each frame. (a) Surface charge density and applied rf voltage, (b) surface potential, (c) E/N, (d) electron density, (e) ionization by bulk electrons, and (f) ionization by secondary electrons.

The local electron density at site B reaches its minimum and ionization processes tend to start earlier at higher rf voltage. These trends are due to the surface voltage at site A reaching its negative peak value earlier at $V_{rf} = 5.6$ kV which leads to a time-shift of electron current extraction and ionization process. For example, the dielectric surface potential at site A reaches its most negative potential at t = 20 ns and 17 ns for $V_{rf} = 1.4$ kV and 5.6 kV, the corresponding ionization source S_e also peaks at t = 21.5 ns and 16 ns, respectively.

Charge collection on the top electrode as a function of dielectric constant ($\varepsilon_r = \varepsilon/\varepsilon_0$) of the insulator between the discharge electrode and rf electrode is shown as a function of time in Fig. 15 for a frequency of 25 MHz. The dielectric properties at site A and ionization characteristics at site B (E/N and ionization sources) and C (electron density) are shown in Fig. 16 for $\varepsilon/\varepsilon_0 = 2$, 5, 10, and 20. Since the intervening dielectric acts as a capacitor whose capacitance scales with ε_r, its charging characteristics should scale with ε_r. That is, the surface charge required to charge the dielectric to the line voltage should increase linearly with ε_r. If we normalize charge collection by ε_r, differences are then attributable to transport processes. In general, charge collected per pulse normalized by ε_r is approximately equal (to within 50%) over a factor of ten in ε_r. This indicates that charge collection, at least for a small number of pulses, is limited by the series capacitance of the dielectric. Integrated charge collection then increases with increasing ε_r. For later pulses normalized charge collection increases with increasing dielectric constant; 2×10^{-12} C/pulse/ε_r with $\varepsilon/\varepsilon_0 = 2$, increasing to 4.5×10^{-12} C/pulse/ε_r with $\varepsilon/\varepsilon_0 = 20$.

The normalized charge density (surface charge density/ε_r), V_{rf}, and local potential at site A for different ε_r are shown in Fig. 16. The normalized charge density collected at site A is essentially the same during the rf period for all values of ε_r. The surface potential on the dielectric reaches a maximum magnitude of 500 V, and as ε_r increases, more charge is required to charge the surface to this potential, thereby necessitating an increase in current density and so electron density. Electron densities at site C reach their maximum

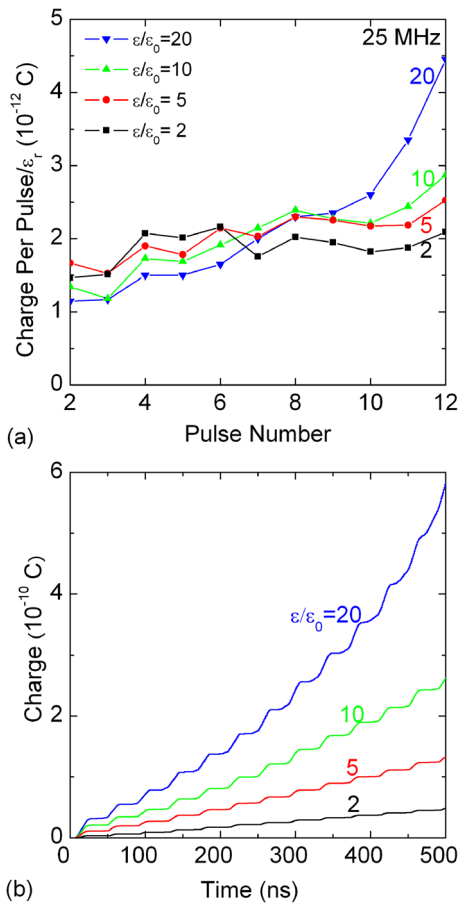

FIG. 15. Charge collection/pulse and total charge collected by the top 2 kV biased electrode as a function of time for 25 MHz with $\varepsilon/\varepsilon_0 = 20$, 10, 5, and 2 with 1.4 kV on the rf electrode. The charge per pulse is normalized by $\varepsilon_r = \varepsilon/\varepsilon_0$.

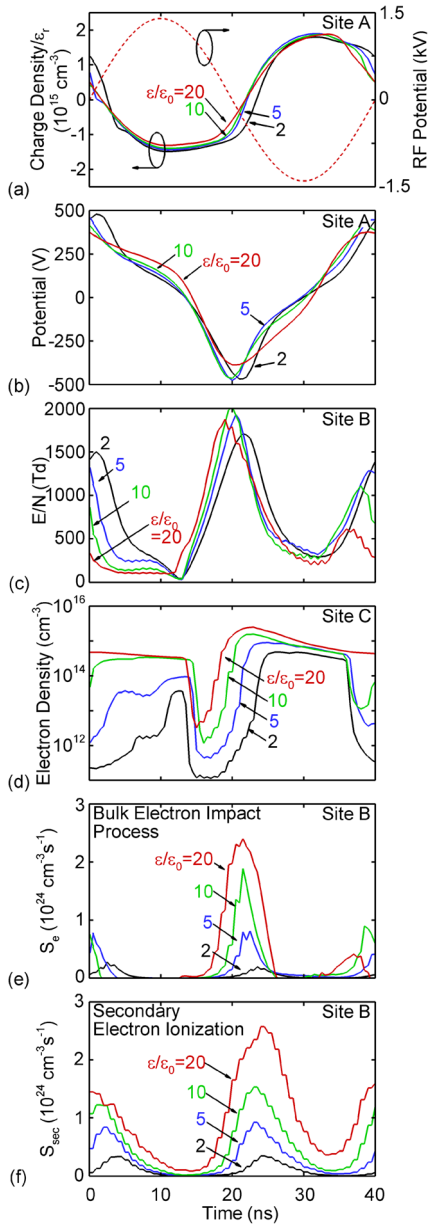

FIG. 16. Surface properties at site A and gas phase properties at sites B and C as a function of time at 25 MHz for $\varepsilon/\varepsilon_0 = 20$, 10, 5, and 2. The location is noted in each frame. (a) Surface charge density normalized by ε_r and rf voltage, (b) surface potential, (c) *E*/*N*, (d) electron density, (e) ionization by bulk electrons, and (f) ionization by secondary electrons.

values when the current is extracted out of the mDBD cavity. Peak electron densities scale nearly linearly with ε_r, up to $10^{15}\,\mathrm{cm}^{-3}$ for $\varepsilon_r = 20$. As $\varepsilon/\varepsilon_0$ decreases from 20 to 2, the dielectric charging time decreases and so the overshoot in electron density is more prominent. The peak value of *E*/*N*, 1800–2000 Td, is largely determined by the nearly constant magnitude of surface potential which occurs when the electrons are expelled out of mDBD cavity. So this peak value is largely determined by the vacuum fields. In spite of the low electron densities in the cavity, the large value of *E*/*N* produces the maximum S_e, up to $2.3 \times 10^{24}\,\mathrm{cm}^{-3}\ \mathrm{s}^{-1}$ for $\varepsilon/\varepsilon_0 = 20$. Ionization by secondary electrons has values that are essentially the same as for ionization by bulk electrons over the entire range of ε_r investigated.

VI. CONCLUDING REMARKS

Dielectric barrier discharges are being used as current sources for charging of surfaces in a variety of applications and digital printing, in particular. Using results from a two-dimensional plasma hydrodynamics model, we investigated the properties of a micro-DBD with an additional charge extraction electrode sustained in atmospheric pressure N_2 with a small O_2 impurity. Properties were investigated as a function of driving voltage, frequency, dielectric constant, and extraction voltage. For the design investigated, the electron density produced within the mDBD cavity can be extracted into a plume that is collected by a dc biased electrode. The value of the extraction bias determines whether the device delivers continuous pulses of extracted current, or transitions to a pulse modulated dc current source. We found that in the pulsed mode, current extraction is ultimately limited by charging of the intervening dielectric—more charge extraction for larger dielectric constants. We also found that the shape of the current pulse is a function of frequency. At high frequencies (tens of MHz), a single current pulse is extracted during each rf cycle. At low frequencies (a few MHz), the current pulse is modulated into individual peaks, produced by successively charging and discharging of the intervening dielectric. Extraction of current from the mDBD cavity can deplete the electron density to such a large extent that the plasma inside the mDBD needs to be re-ignited each rf cycle. The re-ignition is facilitated, in part, by long lived excited states that provide photons which generate secondary electrons from the insides surfaces of the cavity.

ACKNOWLEDGMENTS

This work was supported by HP Research Labs and the HP Labs Innovation Research Program.

[1]C. Penache, C. Gessner, T. Betker, V. Bartels, A. Hollaender, and C.-P Klages, IEE Proc. Nanobiotechnol. **151**, 139 (2004).
[2]S. Kreitz, C. Penache, M. Thomas, and C.-P. Klages, Surf. Coat. Technol. **200**, 676 (2005).
[3]K. H. Schoenbach, M. Moselhy, and W. Shi, Plasma Sources Sci. Technol. **13**, 177 (2004).
[4]N. S. Panikov, S. Paduraru, R. Crowe, P. J. Ricatto, C. Christodoulatos, and K. Becker, IEEE Trans. Plasma Sci. **30**, 1424 (2002).
[5]K. H. Becker, K. H. Schoenbach, and J. G. Eden, J. Phys. D: Appl. Phys. **39**, R55 (2006).
[6]T. S. Cho, S. H. Park, K. H. Becker, and E. E. Kunhardt, IEEE Trans. Plasma Sci. **39**, 1496 (2011).
[7]K. H. Schoenbach, A. El-Habachi, W. Shi, and M. Ciocca, Plasma Sources Sci. Technol. **6**, 468 (1997).
[8]P. S. Kothnur and L. L. Raja, J. Appl. Phys. **97**, 043305 (2005).
[9]S.-J. Park, J. G. Eden, K. Jain, and M. A. Klosner, Jpn. J. Appl. Phys., Part 1 **45**, 8221 (2006).
[10]S. A. Al-Bataineh, E. J. Szili, A. Mishra, S. J. Park, J. G. Eden, H. J. Grisesser, N. H. Voelcker, R. D. Short, and D. A. Steel, Plasma Processess Polym. **8**, 695 (2011).
[11]J. D. Readle, K. E. Tobin, K. S. Kim, J. K. Yoon, J. Zheng, S. K. Lee, S.-J. Park, and J. G. Eden, IEEE Trans. Plasma Sci. **37**, 1045 (2009).
[12]S.-J. Park, P. A. Tchertchian, S. H. Sung, T. M. Spinka, and J. G. Eden, IEEE Trans. Plasma Sci. **35**, 215 (2007).
[13]J. P. Boeuf, J. Phys. D: Appl. Phys. **36**, R53 (2003).
[14]U. Kogelschatz, Plasma Chem. Plasma Process. **23**, 1 (2003).
[15]S. Kanazawa, M. Kogoma, T. Moriwaki, and S. Okazaki, J. Phys. D: Appl. Phys. **21**, 838 (1988).
[16]T. Yokoyama, M. Kogoma, T. Moriwaki, and S. Okazaki, J. Phys. D: Appl. Phys. **23**, 1125 (1990).

[17]A. Fridman, A. Chirokov, and A. Gutsol, J. Phys. D: Appl. Phys. **38**, R1 (2005).
[18]E. E. Kunhardt, IEEE Trans. Plasma Sci. **28**, 189 (2000).
[19]H. H. Kim, Plasma Process. Polym. **1**, 91 (2004).
[20]B. Eliasson, M. Hirth, and U. Kogelschatz, J. Phys. D: Appl. Phys. **20**, 1421 (1987).
[21]G. Borcia, C. A. Anderson, and N. M. D. Brown, Plasma Sources Sci. Technol. **12**, 335 (2003).
[22]M. Sira, D. Trunec, P. Stahel, V. Bursikova, Z. Navratil, and J. Bursik, J. Phys. D: Appl. Phys. **38**, 621 (2005).
[23]Z. Fang, X. Xie, J. Li, H. Yang, Y. Qiu, and E. Kuffel, J. Phys. D: Appl. Phys. **42**, 085204 (2009).
[24]J. Meunier, Ph. Belenguer, and J. P. Boeuf, J. Appl. Phys. **78** (2), 731 (1995).
[25]M. G. Kong, G. Kroesen, G. Morfill, T. Nosenko, T. Shimizu, J. van Dijk, and J. L. Zimmermann, New J. Phys. **11**, 115012 (2009).
[26]H. Ayan, G. Fridman, A. F. Gutsol, V. N. Vasilets, A. Fridman, and G. Friedman, IEEE Trans. Plasma Sci. **36**, 504 (2008).
[27]N. Lucas, A. Hinze, C. P. Klages, and S. Büttgenbach, J. Phys. D: Appl. Phys. **41**, 194012 (2008)
[28]J. Zhang, Y. H. Wang, and D. Z. Wang, Phys. Plasmas **17**, 043507 (2010).
[29]A. Chirokov, A. Gutsol, A. Fridman, K. D. Sieber, J. M. Grace, and K. S. Robinson, Plasma Chem. Plasma Process. **26**, 127 (2006).
[30]L. Stollenwerk, J. G. Laven, and H. G. Purwins, Phys. Rev. Lett. **98**, 255001 (2007).
[31]R. Fotland, E. Hanson, N. Leoni, and P. McClelland, U.S. patent 7,623,144 (24 November 2009).
[32]N. J. Leoni, O. Gila, M. H. Lee, and E. G. Hanson, U.S. patent 2009/0033735 (5 February 2009).
[33]M. W. Brennan, W. G. Read, and S. Read, U.S. patent 6,386,684 (14 May 2002).
[34]G. Bauville, B. Lacour, L. Magne, V. Puech, J. P. Boeuf, E. Munoz-Serrano, and L. C. Pitchford, Appl. Phys. Lett. **90**, 031501 (2007).
[35]J. S. Sousa, G. Bauville, B. Lacour, V. Puech, M. Touzeau, and L. C. Pitchford, Appl. Phys. Lett. **93**, 011502 (2008).
[36]S. Müller, R. J. Zahn, and J. Grundmann, Plasma Process. Polym. **4**, S1004 (2007).
[37]D. Petrović, T. Martens, J. van Dijk, W. J. M. Brok, and A. Bogaerts, J. Phys. D: Appl. Phys. **42**, 205206 (2009).
[38]J. Shin and L. L. Raja, J. Appl. Phys. **94**, 7408 (2003).
[39]Q. Wang, J. Sun, and D. Wang, Phys. Plasmas **18**, 103504 (2011)
[40]X. Duan, F. He, and J. Ouyang, Plasma Sources Sci. Technol. **21**, 015008 (2012).
[41]B. Lay, R. S. Moss, S. Rauf, and M. J. Kushner, Plasma Sources Sci. Technol. **12**, 8 (2003).
[42]Z. Xiong and M. J. Kushner, J. Phys. D: Appl. Phys. **43**, 505204 (2010).
[43]D. L. Scharfetter and H. K. Gummel, IEEE Trans. Electron Devices. **ED-16**, 64 (1969).
[44]M. J. Kushner, J. Appl. Phys. **95**, 846 (2004).
[45]N. Y. Babaeva and M. J. Kushner, Plasma Sources Sci. Technol. **20**, 035017 (2011).
[46]Y. Akishev, M. Grushin, V. Karalnik, A. Petryakov, and N. Trushkin, J. Phys. D: Appl. Phys. **43**, 215202 (2010).
[47]I. Radu, R. Bartnikas, and M. R. Wertheimer, IEEE Trans. Plasma Sci. **31**, 1363 (2003).
[48]A. A. Ionin, Y. M. Klimachev, A. A. Kotkov, I. V. Kochetov, A. P. Napartovich, L. V. Seleznev, D. V. Sinitsyn, and G. D. Hager, J. Phys. D **36**, 982 (2003).